Systematic investigations on the coating degradation mechanism during the steam oxidation of Cr-coated Zry-4 at 1200 °C

Junkai Liu [a,b,*], Martin Steinbrück [a], Mirco Große [a], Ulrike Stegmaier [a], Chongchong Tang [a], Di Yun [b,c,*], Jianqiao Yang [c], Yanguang Cui [d], Hans Jürgen Seifert [a]

[a] Institute for Applied Materials (IAM), Karlsruhe Institute of Technology (KIT), D-76021 Karlsruhe, Germany
[b] School of Nuclear Science and Technology, Xi'an Jiaotong University, Xi'an 710049, China
[c] Key Laboratory of Thermo-Fluid Science and Engineering of MOE, School of Energy and Power Engineering, Xi'an Jiaotong University, Xi'an 710049, China
[d] Shanghai Nuclear Engineering Research & Design Institute, Shanghai 200233, China

ARTICLE INFO

Keywords:
Accident-tolerant fuel (ATF) cladding
Cr coating
High-temperature steam oxidation
Diffusion
Oxidation kinetics transition
Coating degradation

ABSTRACT

The isothermal oxidation behavior of the Cr-coated Zircaloy-4 at 1200 °C in steam is comprehensively investigated. Oxidation kinetics transition is observed when outward diffusion of Zr and precipitation of ZrO_2 along the Cr coating grain boundaries are reaching the Cr_2O_3/Cr interface. The outward diffused Zr reduces the Cr_2O_3 scale to Cr. Pores form on the Cr_2O_3/Cr interface and inside the Cr_2O_3 scale after transition. These interfacial pores affect the oxidation mechanism of the Cr-coated Zry-4. The coating failure and the oxidation of the Zry-4 substrate occur when the thickness of the outer Cr_2O_3 scale decreases to a certain value.

1. Introduction

After the Fukushima nuclear power plant accidents in 2011, the concept of Accident-tolerant fuels (ATFs) was proposed to improve the safety of nuclear reactors under design basic accident (DBA) and beyond design basic accident (BDBA) conditions by improving or replacing the current Zircaloy cladding—UO_2 fuel system [1–4]. Among different ATF concepts, Zircaloy substrates with surface protective coatings have attracted much attention owing to their low R&D costs and short R&D time [5–13]. Among the numerous candidate materials for surface coatings on Zircaloy, pure Cr is considered as the most promising coating material due to its excellent oxidation resistance [14] and adhesion property with Zircaloy substrate [15], relative low thermal neutron absorption cross-section [6], favorable thermo-mechanical properties [15–17], and irradiation resistance [18,19]. Up to date, the oxidation behavior and oxidation mechanism of the Cr-coated Zircaloy under high-temperature steam atmospheres have been extensively investigated by different research groups, and almost all the results show that the Cr coating can effectively protect the Zircaloy substrate from oxidation during the steam exposure up to 1200–1300 °C for a certain time [15,20–25].

However, although a large number of oxidation experiments with Cr-coated Zircaloy were conducted under steam atmospheres at different temperatures, the coating degradation mechanism of the Cr-coated Zircaloy and the oxidation kinetics transition mechanism during the high-temperature steam oxidation are still ambiguous. Up to present, there are mainly two widely accepted mechanisms related to coating failure and degradation. One is proposed by Brachet et al. [25], the mechanism focuses on the failure of the unoxidized Cr coating beneath the outer Cr_2O_3 scale. During steam oxidation, Zr diffuses from the Zircaloy substrate towards the outer Cr coating and is further oxidized into ZrO_2 on the Cr grain boundaries. The ZrO_2 grains inside the Cr coating connect with each other and finally form networks, which can act as paths for the inward diffusion of oxygen. Then the coating failure occurs and a large amount of oxygen reaches the Zircaloy substrate. Another mechanism is proposed by Han et al. [20,21] concentrating on the failure of the outer dense Cr_2O_3 scale of the Cr coating during oxidation. The thickness of the Cr_2O_3 scale first increases by the oxidation of Cr coating. When the Cr coating is completely oxidized and the thickness of the Cr_2O_3 scale reaches its maximum value, the Cr_2O_3 scale will be reduced by the redox reaction between Cr_2O_3 and the Zircaloy substrate. The thickness decrease of the Cr_2O_3 scale results in the fast inward diffusion of oxygen into the inner coating and the substrate through the outer Cr_2O_3 scale. In our previous work on the transient oxidation behavior of the Cr-coated Zircaloy under steam atmosphere up to 1600 °C [23] and in later studies of Han et al. [20] and

* Corresponding authors at: School of Nuclear Science and Technology, Xi'an Jiaotong University, Xi'an 710049, China.
E-mail addresses: k611478@stu.xjtu.edu.cn (J. Liu), diyun1979@xjtu.edu.cn (D. Yun).

other researchers [26], both the outward diffusion and oxidation of Zr along the Cr grain boundaries and the thickness decrease of the outer dense Cr_2O_3 scale were simultaneously observed. Nevertheless, the connection between these two critical phenomena has never been investigated and discussed. So, the first question arises if there is any relationship between the thickness decrease of the outer Cr_2O_3 scale and the formation of the ZrO_2 networks inside the inner unoxidized Cr coating.

Moreover, the mechanism of the thickness decrease of the outer Cr_2O_3 scale during steam oxidation needs to be studied further. During the transient steam oxidation of Cr-coated Zry-4, we observed that the thickness of the Cr_2O_3 scale began to decrease although the Cr coating is not completely oxidized into Cr_2O_3. There was no ZrO_2 layer formed on the Zircaloy substrate when the Cr_2O_3 scale was reduced [23]. These two phenomena are inconsistent with the mechanism proposed by Han et al. [21] that the Cr_2O_3 scale is reduced by the reaction between Cr_2O_3 and the Zircaloy substrate. Hence, the second question is whether there are other factors that cause the thickness decrease of the Cr_2O_3 scale. Besides, in our previous work about the isothermal steam oxidation of the Cr-coated Zry-4 at 1000 °C [22], we have observed the formation of pores on the Cr_2O_3/Cr interface and we have emphasized the importance of these interfacial pores to the oxidation behavior of the Cr coating. The Cr_2O_3/Cr interface, especially with pores on it, acts as a physical bond and connects the outer Cr_2O_3 scale and the inner unoxidized Cr coating (with ZrO_2 in it). Therefore, the third question is whether these interfacial pores are related to the reduction of the Cr_2O_3 scale, the formation of the ZrO_2 networks inside the Cr coating, and the oxidation kinetics transition of the Cr-coated Zircaloy.

In order to answer the three questions raised above, the isothermal oxidation experiments of the Cr-coated Zircaloy under steam atmosphere at 1200 °C were repeated in this work using a horizontal tube furnace at KIT. All the samples were pushed from the cold zone (room temperature) into the hot furnace (1200 °C) before oxidation and quenched in argon after oxidation to avoid the diffusion of atoms during the heating and cooling stages. Different to other researchers' works, in the current work, more attention was paid to the relationship between the Cr_2O_3 scale reduction, the outward diffusion and selective oxidation of Zr on the Cr grain boundaries, the microstructural evolution behavior of the Cr_2O_3/Cr interface especially the evolution of pores on the Cr_2O_3/Cr interface, and the oxidation kinetics transition. Based on these analyses, a coating degradation and failure mechanism and a mechanism of the oxidation kinetics transition are proposed.

2. Materials and methods

The Zircaloy substrate materials used in this paper are Zry-4 (Zr-1.5Sn-0.2Fe-0.1Cr) plates with length 15 mm, width 10 mm and thickness 0.65 mm. A 2 mm diameter hole was drilled in each sample for suspension. The Cr coating was deposited on all the six surfaces of the samples by magnetron sputtering at Oerlikon Balzers Coating Germany GmbH using an Oerlikon BAI830C coating machine. Two sputtering Cr sources with a power of 8 kW were equipped on the coating machine. The coating deposition process mainly included vacuuming the deposition chamber, heating, ion etching of the sample surfaces, spraying Cr coating, and cooling. Deposition temperature was below 300 °C. The deposition time of the Cr coating was 430 min resulting in a coating thickness of ~17 μm.

A horizontal tube furnace, named BOX rig, was used to conduct the isothermal steam oxidation tests of the Cr-coated Zry-4 at 1200 °C. The main three parts of the BOX rig are a gas mixer and evaporator (Bronkhorst®) which supplies the steam and argon during oxidation, the horizontal tube furnace with alumina reaction tube, and a quadrupole mass spectrometer (MS, IPI GAM3000) which is connected with the outlet of the furnace. More details about the BOX rig are provided in our previous papers [27,28]. How the samples were suspended in the furnace during oxidation was described in another paper [23] with a detailed schematic of the furnace part. During the oxidation tests, the temperature of the steam atmosphere was measured close to the sample by a thermocouple, which was installed inside the furnace. Ar, H_2O, H_2 as well as other potential impurity gases were in situ analyzed by MS.

Before steam oxidation, the furnace was first heated up to 1200 °C with a heating rate of 10 K/min and then was kept at 1200 °C. Argon with flow rate of 20 L/h was injected in the furnace during the whole oxidation test process. When the furnace temperature reached 1200 °C, steam with a flow rate of 20 g/h was introduced into the furnace resulting in a water steam concentration of ~55.4 mol%. When the steam flow was stable and there was almost no nitrogen or oxygen remaining in the furnace, the Cr-coated Zry-4 sample was moved into the furnace using a sample lock system (see in [23]). After oxidation for the pre-defined time, the sample was pulled out of the hot and into the cooling region of BOX using the sample lock and then quenched in flowing argon. After cooling for ~5 min, a new sample was exchanged via the sample lock and the oxidation process was repeated. The isothermal oxidation times of each sample in this paper are listed in Table 1. The current experimental design with very fast heating and cooling rate before and after oxidation can effectively avoid the Zr—Cr interdiffusion between the coating and the substrate during the heating and cooling stages. Hydrogen produced by the oxidation reaction was in situ analyzed by the MS. The weights of the samples before and after oxidation were measured with a high-precision analytical balance (accuracy 0.01 mg).

X-ray diffraction (XRD, PANalytical Empyrean) with a Cu Kα radiation source (λ 1.54 Å) was used to study the surface phases (only several microns depth) of the samples with a scanning range of 20–110° and scanning step 0.01313°. The cross-sectional microstructures of the Cr-coated Zry-4 samples after oxidation were characterized by optical microscopy (OM, Reichert-Jung MeF3) and scanning electron microscopy (SEM, PhilipsXL30S) equipped with energy dispersive X-ray spectroscopy (EDS). Specimens for cross-sectional characterization were prepared by embedding in epoxy resin, grinding, polishing, ultrasonically cleaning, and drying. Transmission electron microscopy (TEM, JEOL JEM-2100) was utilized to further study the microstructures of the Cr_2O_3 scale and the Cr_2O_3/Cr interface. Two TEM specimens were lifted on both surfaces of the #G sample after oxidation for 90 min by a focused ion beam (FIB, Helios Nanolab600i) system.

3. Results

3.1. Hydrogen release and weight gain

Fig. 1 shows the hydrogen release rate curves and the weight gain data of the nine Cr-coated Zry-4 samples during the isothermal steam oxidation at 1200 °C for different times. The hydrogen mass flow rate values in Fig. 1(a) indicate the real-time oxidation rates. As can be seen in Fig. 1(a), all the hydrogen release curves of different samples are in similar trends with the oxidation rate being large at the initial oxidation stage and then gradually decreasing with the increase of the oxidation time. The small value differences of hydrogen mass flow rate between different samples should be due to the error in the measurement process by MS because of the very small concentration of hydrogen (only several hundreds ppm) during the oxidation. The hydrogen release curves reach a minimum value after ~30 min indicating an oxidation kinetics transition. There are small differences on the transition time between different samples. The integrated hydrogen release curve versus oxidation time of the #I sample with the longest oxidation time is shown in

Table 1
The oxidation times of each sample.

Samples	#A	#B	#C	#D	#E	#F	#G	#H	#I
Oxidation time (min)	5	10	20	30	45	60	90	120	180

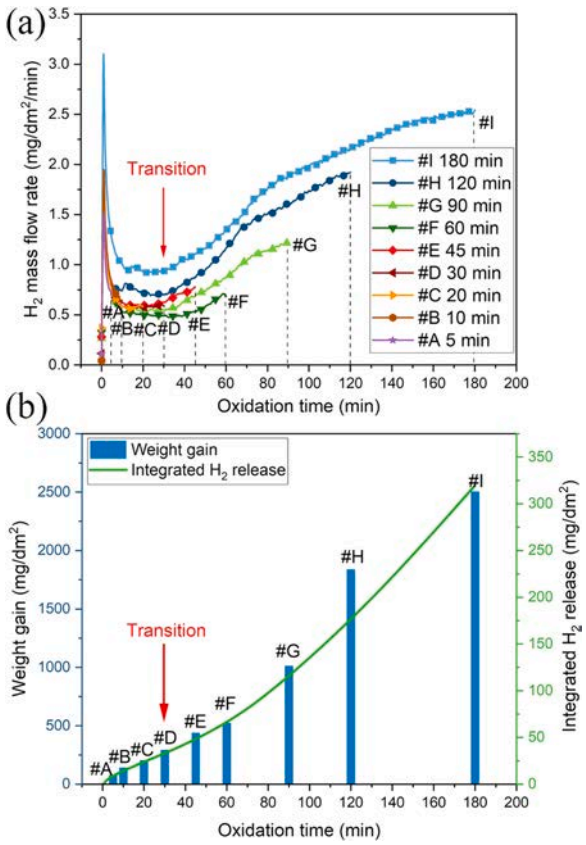

Fig. 1. (a) Hydrogen release behavior of the Cr-coated Zry-4 samples during the isothermal steam oxidation at 1200 °C; (b) the integrated hydrogen release of #I sample and weight gain data of each sample.

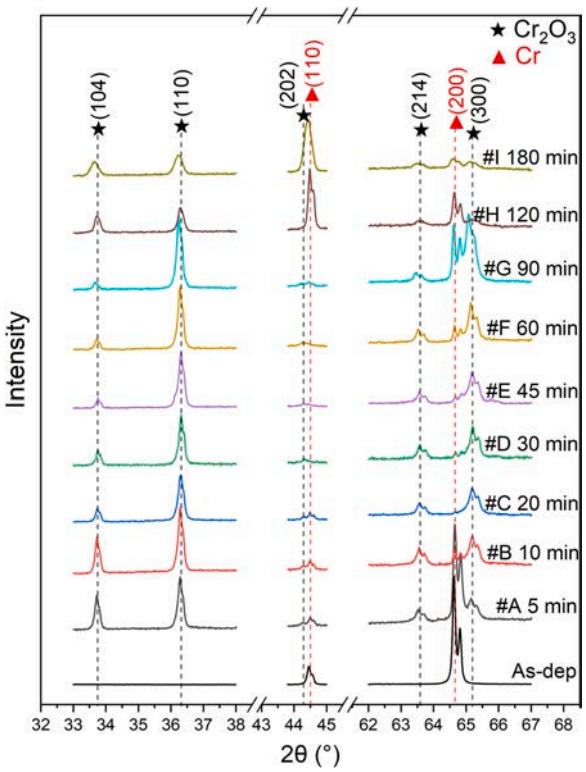

Fig. 2. XRD patterns of the Cr-coated Zry-4 samples before and after steam oxidation for different times.

Fig. 1(b) and this curve is in good agreement with that of the oxidation weight gain data in Fig. 1(b) (the weight gain of the sample should be 8 times the mass of hydrogen released). It can be clearly observed in Fig. 1 (b), that the oxidation kinetics transforms from a parabolic law to an accelerating law at ~30 min

3.2. XRD results of the Cr-coated Zry-4 samples before and after oxidation

Fig. 2 shows the XRD patterns of the Cr-coated Zry-4 samples before and after steam oxidation for different times. To better show the XRD results, only some representative peaks of Cr and Cr_2O_3 are presented in Fig. 2. Only the Cr peaks are visible for the as-deposited Cr coating. Peaks of Cr_2O_3 appear in all samples after steam oxidation. However, after steam oxidation, the intensity of the Cr peaks first decreases with the increase of the oxidation time and they almost disappear after oxidation for 30 min. Then the Cr peaks appear again after oxidation for ~60 min, and the intensity of the Cr (110) peak increases with oxidation time. After oxidation for 120 min and 180 min, the intensity of the Cr (110) peak is much higher than the Cr_2O_3 (104) and (110) peaks.

3.3. The cross-sectional microstructures after steam oxidation

Fig. 3 shows the cross-sectional and surface microstructures of the as-deposited Cr coating on the Zry-4 substrate, which were also studied and reported in our previous work [23]. The average thickness of the as-deposited Cr coating is ~17.4 μm (Fig. 3(a)). The average grain size of the Cr coating is ~2 μm (Fig. 3(b)).

3.3.1. Before transition, oxidation time 5–30 min

Fig. 4 shows the cross-sectional SEM micrographs of four Cr-coated Zry-4 samples after oxidation for 5 min, 10 min, 20 min, and 30 min in steam at 1200 °C. These four samples are all in the stage before transition. As shown in Fig. 4(a)—(d), all these four samples have the typical three-layer structure with outermost Cr_2O_3, middle Cr, and inner $ZrCr_2$, which has been widely reported and discussed by other researchers after oxidation of Cr-coated Zr alloys [20,22,25,29,30]. The average thickness of the whole coating and every sublayer of different samples were measured, the results are shown in Fig. 5. The thickness evolution of the individual sublayers of the #A—#D samples can be summarized as follows: the thickness of the Cr_2O_3 scale and the $ZrCr_2$ layer increases while the thickness of the unoxidized Cr coating layer decreases with longer oxidation time. Fig. 4(e)—(g) display the EDS maps of Zr and Cr of the #B—#D samples, with the regions of the EDS maps in Fig. 4(e), (f), and (g) marked by the yellow squares in Fig. 4(b), (c), and (d), respectively. In Fig. 4(e) and (f), Cr-rich precipitates are distributed inside the Zry-4 substrate, which are due to the inward diffusion of Cr from the coating to substrate. Moreover, Zr-rich networks are distributed inside the unoxidized Cr coating in Fig. 4(e)—(g). These Zr-rich networks were identified as ZrO_2 by other researchers [22,25] and also by TEM results in the next section. The formation mechanism should be attributed to the outward diffusion and selective oxidation of Zr on the Cr grain boundaries [22]. To be more accurate, the designation $Cr(ZrO_2)$ (Cr layer which contains ZrO_2) is used to describe the unoxidized Cr coating. It is worth mentioning that the diffusion distance of Zr inside the Cr coating increases with oxidation time. The position evolution of these ZrO_2 precipitates is displayed in Fig. 5 by blue stars. Before transition, all these ZrO_2 precipitates in the four samples have not reached the Cr_2O_3/Cr interface. After oxidation for 30 min (#D in Fig. 4 (g)), these ZrO_2 precipitates are very close to the Cr_2O_3/Cr interface.

3.3.2. After transition, oxidation time 45–90 min

Fig. 6 shows the cross-sectional OM images of the #E, #F, and #G samples after isothermal steam oxidation for 45 min, 60 min, and 90 min, respectively. According to the hydrogen release curves in Fig. 1

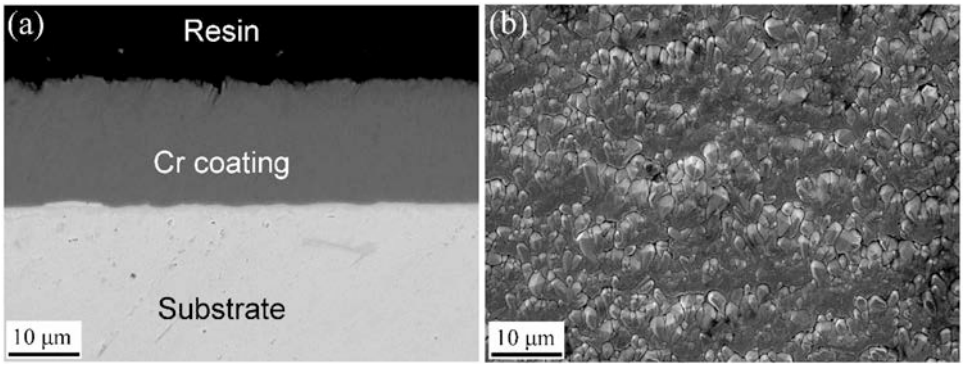

Fig. 3. The SEM images of the as-deposited Cr-coating on the Zry-4 substrate: (a) cross-sectional microstructure; (b) surface microstructure.

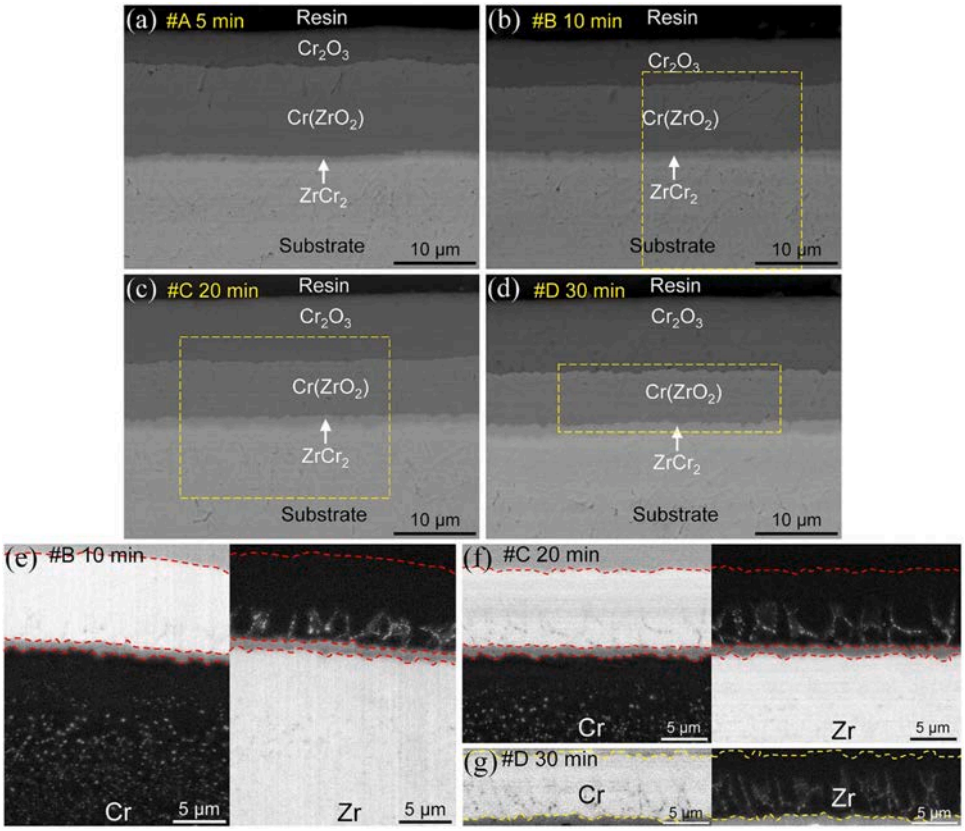

Fig. 4. The cross-sectional SEM images of the Cr-coated Zry-4 samples before transition: (a)—(d) BSE images of the #A, #B, #C and #D samples; (e)—(g) EDS maps of Cr and Zr inside the yellow squares in (b), (c) and (d).

(a), during the steam oxidation of these three samples, the oxidation kinetics transition has occurred. As can be seen in Fig. 6, the thickness of the Cr_2O_3 scales varied on both surfaces of the samples. In addition, the thickness of Cr_2O_3 scales on each surface is not uniform at different locations. We have repeated these three tests and the results indicated that the thickness of the surface oxide is independent of whether this surface is facing the steam flow during steam oxidation or not. After transition, there is an α-Zr(O) layer formed beneath the surface coating due to the inward diffusion of O into the Zircaloy substrate. The absorption of O by Zircaloy substrate should be the direct cause for the oxidation kinetics transition. Interestingly, the thinner the Cr_2O_3 scale, the thicker the α-Zr(O). Moreover, the thickness of the α-Zr(O) layer increases with the increase of the oxidation time.

Fig. 7 shows the cross-sectional SEM images of the #E and #F samples together with the corresponding EDS maps. The most intuitive difference of the cross-sectional microstructures between the samples before (Fig. 4) and after transition (Fig. 7) is the transformation of the Cr_2O_3/Cr and the $ZrCr_2$/Zr interfaces from flat to wavy. After transition, the coating keeps the same three-layer structure as the samples before transition. The thickness evolution of each sublayer of these three samples is also summarized in Fig. 5. With the oxidation time increasing from 30 min to 45 min and the occurrence of the transition, the thickness of the outer Cr_2O_3 scale significantly decreases while the thickness of the $Cr(ZrO_2)$ layer does not change too much. This indicates that the transition is directly related to the thinning of the Cr_2O_3 scale. When the oxidation time further increases to 60 min and 90 min (Fig. 5), the thickness of the $Cr(ZrO_2)$ layer slightly increases but there is no large change of the Cr_2O_3 scale thickness. After transition, as shown in Fig. 7, pores are observed on the Cr_2O_3/Cr interfaces (indicated by the yellow arrows). Compared with the #E sample in Fig. 7(a), the density of the

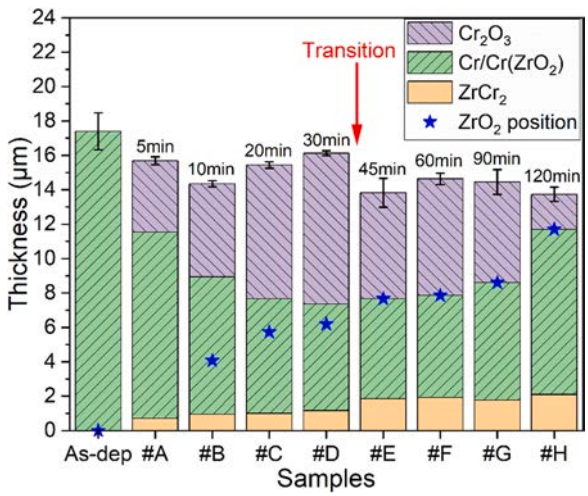

Fig. 5. Thickness evolution of the coating and each sublayer within the coating together with the position of the ZrO_2 precipitates on the Cr grain boundaries of different samples.

pores on the Cr_2O_3/Cr interface of the #F sample in Fig. 7(c) is higher. Moreover, a few pores are also observed inside the Cr_2O_3 scale (see in Fig. 7(e)). According to the EDS maps of the Cr(ZrO_2) layer in Fig. 7(b) and (f), a significant difference is observed on the Cr(ZrO_2) layer between the samples before (Fig. 4(e)—(g)) and after transition: the ZrO_2 precipitates in the Cr coating have reached the Cr_2O_3/Cr interface after transition. These ZrO_2 networks distribute throughout the entire Cr coating and connect the outer Cr_2O_3 scale and the inner $ZrCr_2$ layer. Some changes have also taken place on the microstructure of the $ZrCr_2$ layer (Fig. 7(b) and (f)). The $ZrCr_2$ phase just beneath the outer ZrO_2 precipitates has transformed into Zr, also there are Zr particles distributed inside the $ZrCr_2$ layer. Therefore, the continuous $ZrCr_2$ layer transforms to a discontinuous one. As for the precipitates inside the substrate, small Cr-rich precipitates have formed in the #F sample after 60 min of oxidation (Fig. 7(d)).

The cross-sectional SEM micrographs after oxidation for 90 min under steam atmosphere at 1200 °C as well as corresponding EDS maps are shown in Fig. 8. As can be seen in Fig. 8(a), the nonuniform thickness of the outer Cr_2O_3 scale is very distinct. This type of nonuniformity should be related to the wavy inner Cr_2O_3/Cr interface because the outer surface of the Cr_2O_3 scale is flat. In Fig. 8(b), the Cr-rich precipitates inside the substrate transformed from small bulbiform particles to large and clubbed precipitates. Moreover, Fe also segregated inside these Cr-rich precipitates, which was also observed in our previous work [23]. As shown in the SEM image with large magnification in Fig. 8(c), a large number of pores are distributed inside the Cr_2O_3 scale and at the Cr_2O_3/Cr interface. Compared with the #E and #F samples in Fig. 7, the concentration of the pores inside the Cr_2O_3 scale is much larger in the #G sample while the number of pores at the Cr_2O_3/Cr interface is reduced.

The elemental distribution on the junction of the thick and thin oxide layer is further characterized by EDS maps. As can be seen in Fig. 8(d), the thickness of the Cr_2O_3 scale is directly associated with the outward diffusion of Zr. ZrO_2 networks distributed inside the Cr layer beneath the thin Cr_2O_3 scale while beneath the thick Cr_2O_3 scale there are no obvious ZrO_2 precipitates. The wave-like Cr_2O_3/Cr interface was also observed in the #G sample in Fig. 8(e), and there are ZrO_2 precipitates

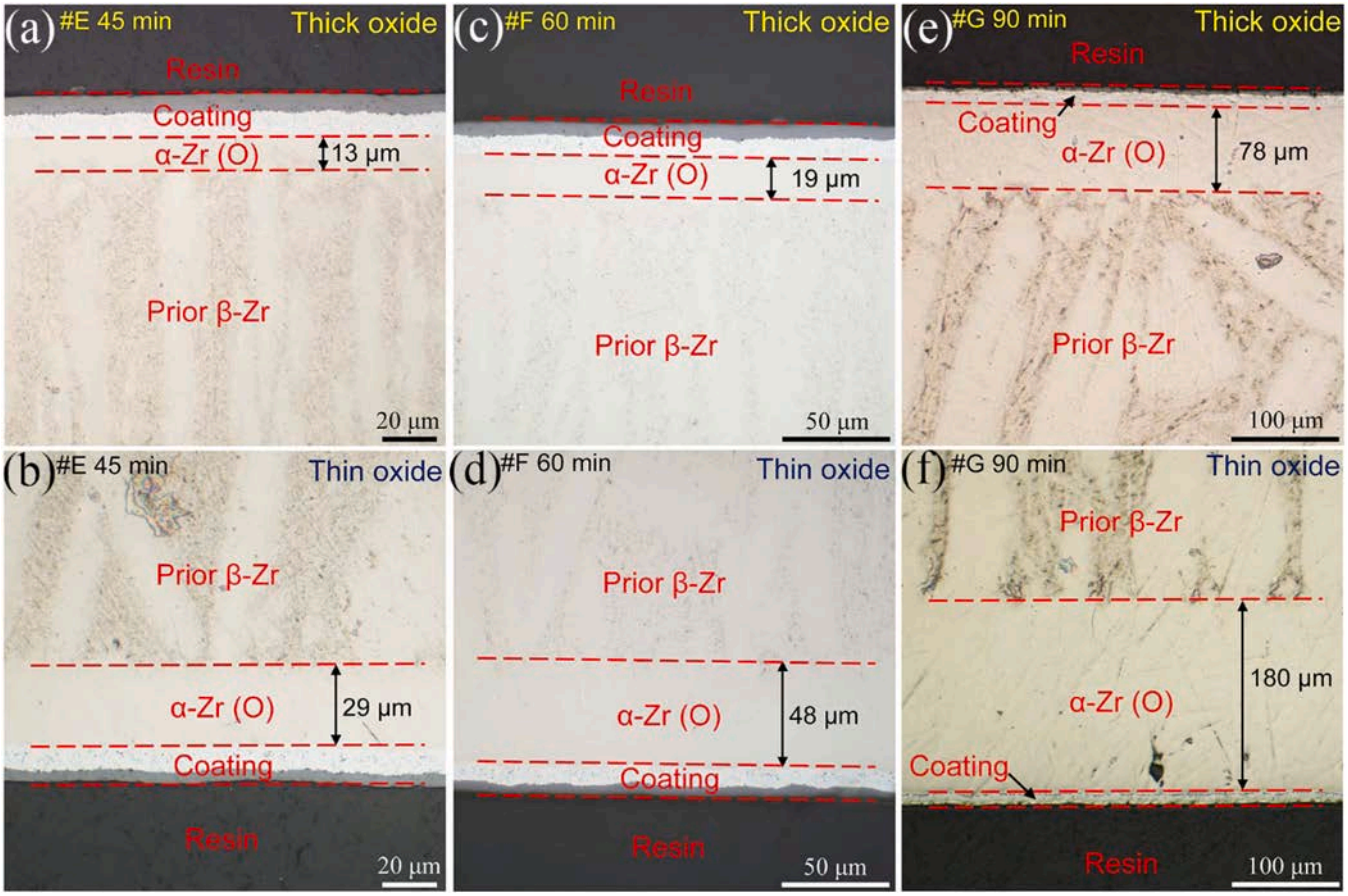

Fig. 6. The cross-sectional OM images on both two sides of the Cr-coated Zry-4 samples after steam oxidation: (a) and (b) #E sample; (c) and (d) #F sample; (e) and (f) #G sample.

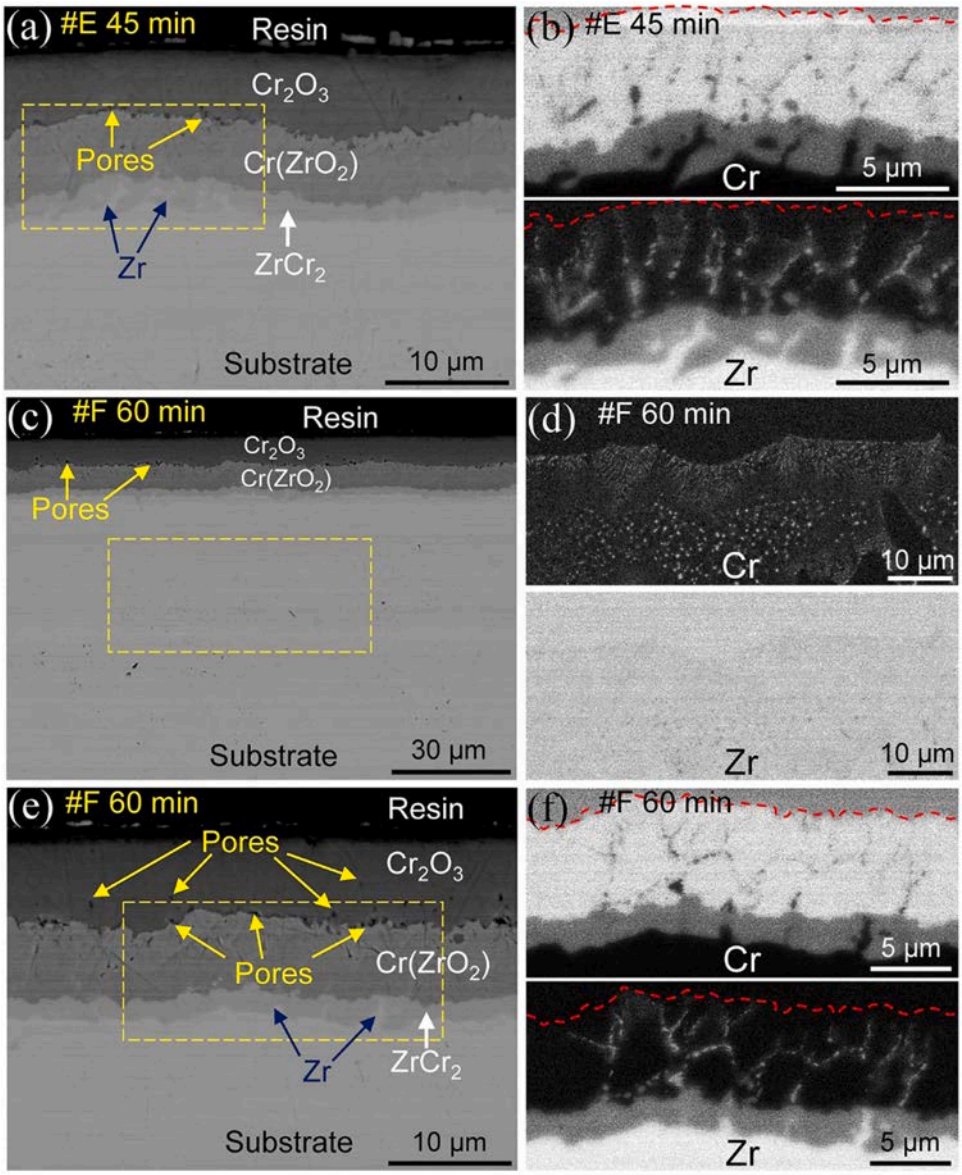

Fig. 7. The cross-sectional SEM images of the Cr-coated Zry-4 samples after steam oxidation: (a) BSE image of the #E sample; (b) EDS maps of the $Cr(ZrO_2)$ layer in the #E sample; (c) BSE image of the #F sample in small magnification; (d) EDS maps of the substrate in the #F sample; (e) BSE image of the #F sample in large magnification; (f) EDS maps of the $Cr(ZrO_2)$ layer in the #F sample. The regions of EDS maps are indicated by the yellow squares. (For interpretation of the references to colour in this figure legend, the reader is referred to the web version of this article.)

distributed inside the Cr coating beneath the wave crest as seen in the EDS maps in Fig. 8(f). In summary, the inhomogeneous outward diffusion of Zr inside the Cr coating leads to the formation of the outer nonuniform Cr_2O_3 scale and the wavy Cr_2O_3/Cr interface. It is worth mentioning that there are large pores (indicated by yellow arrows) linearly distributed inside the Cr_2O_3 scale (Fig. 8(e)). Almost all the linearly arranged pores are distributed above the wave crest of the Cr_2O_3/Cr interface. To be more specific, these pores in the Cr_2O_3 are distributed mainly above the position of the ZrO_2 precipitates in the unoxidized Cr coating according to Fig. 8(e) and Fig. 8(f).

3.3.3. After transition, oxidation time 120–180 min

Fig. 9 shows the cross-sectional OM images of the #H and #I samples after oxidation for 120 min and 180 min under steam atmosphere at 1200 °C, respectively. When the oxidation time increases to 120 min, as can be seen in Fig. 9(a), the coating failure has occurred and most regions of the Zircaloy substrate have been attacked by steam. However, some regions of the substrate remain as metal and are not oxidized into ZrO_2. After oxidation for 180 min, all the substrate beneath the surface coating has been oxidized (Fig. 9(b)), and the average thickness of the ZrO_2 layer is much larger than that of the #H sample. According to the OM images, the microstructures of the surface coatings in #H and #I samples are similar and mainly consist of a bright metal phase. This result is also consistent with the XRD results (Fig. 2) that showed mainly Cr phase inside the surface coating of the #H and #I samples.

Fig. 10 shows the SEM images together with EDS results of the #H sample after oxidation for 120 min Fig. 10(a)—(d) are at the position where the substrate beneath the surface coating has been oxidized. In Fig. 10(a), although the surface coating has lost its protective function, no spallation or cracking of the coating is observed. According to the EDS maps in Fig. 10(b), there is a thin Cr_2O_3 layer remaining at the outermost side of the coating. A large number of ZrO_2 networks are distributed inside the unoxidized Cr layer. Similar to the #G sample, Cr and Fe-rich large clubbed precipitates distribute inside the substrate. As can be seen in Fig. 10(c) and (d), the surface coating transformed to a quadruple-layer structure after coating failure. The four layers from the outer side to the inner side of the coating are Cr_2O_3, $Cr(ZrO_2)$, ZrO_2, and $Cr(ZrO_2)$. The thickness of the outer Cr_2O_3 scale significantly decreased while the thickness of the middle $Cr(ZrO_2)$ layer increased. Different from the former samples before coating failure, in the #H sample, with the substrate being oxidized, the $ZrCr_2$ layer disappears and is partly oxidized and converted into ZrO_2 and Cr. This phenomenon was also

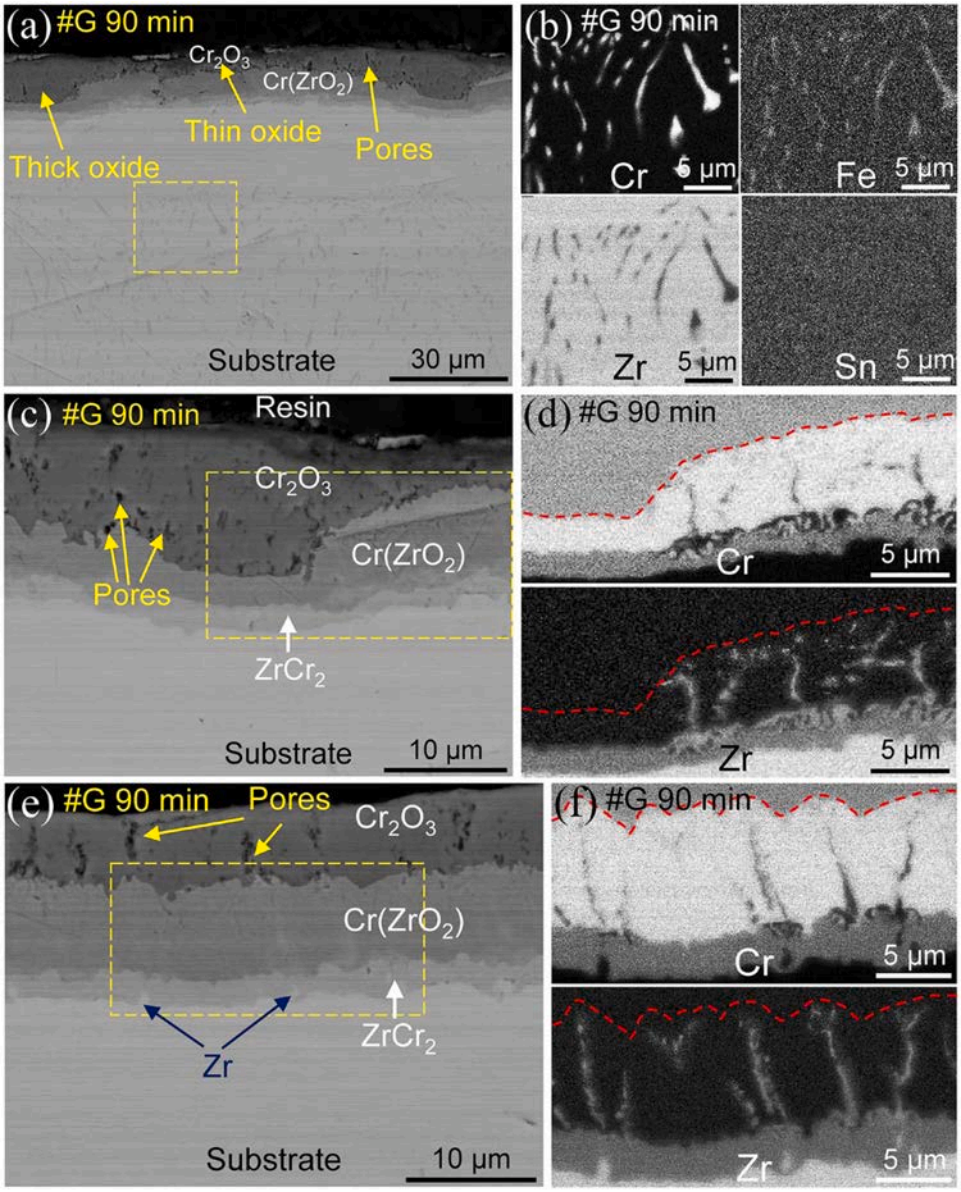

Fig. 8. The cross-sectional SEM images of the Cr-coated Zry-4 samples after steam oxidation: (a) BSE image of the #G sample in small magnification; (b) EDS maps of the substrate in the #G sample; (c) BSE image of the #G sample in large magnification; (d) EDS maps of the Cr (ZrO_2) layer in (c); (e) BSE image of the #G sample at the position with wave-like interface; (f) EDS maps of the Cr(ZrO_2) layer in (e). The regions of EDS maps are indicated by the yellow squares. (For interpretation of the references to colour in this figure legend, the reader is referred to the web version of this article.)

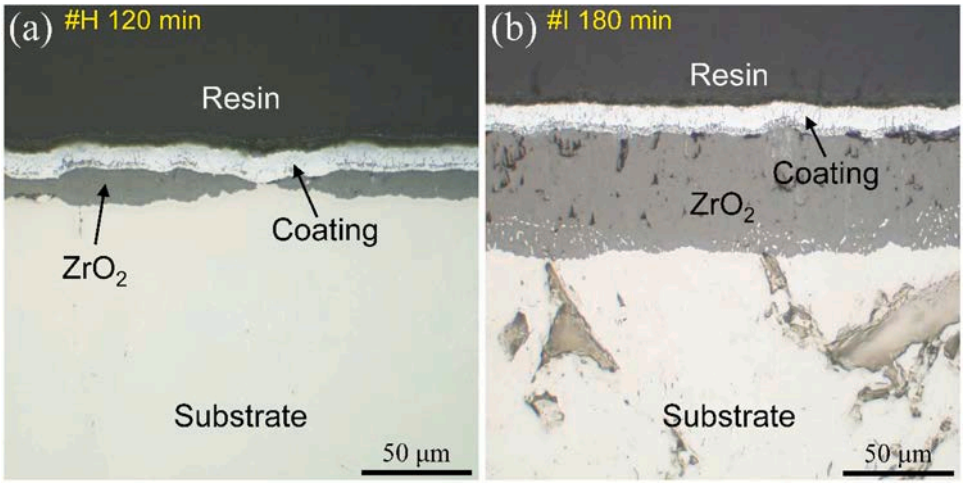

Fig. 9. The cross-sectional OM images of the Cr-coated Zry-4 samples after steam oxidation: (a) #H sample; (b) #I sample.

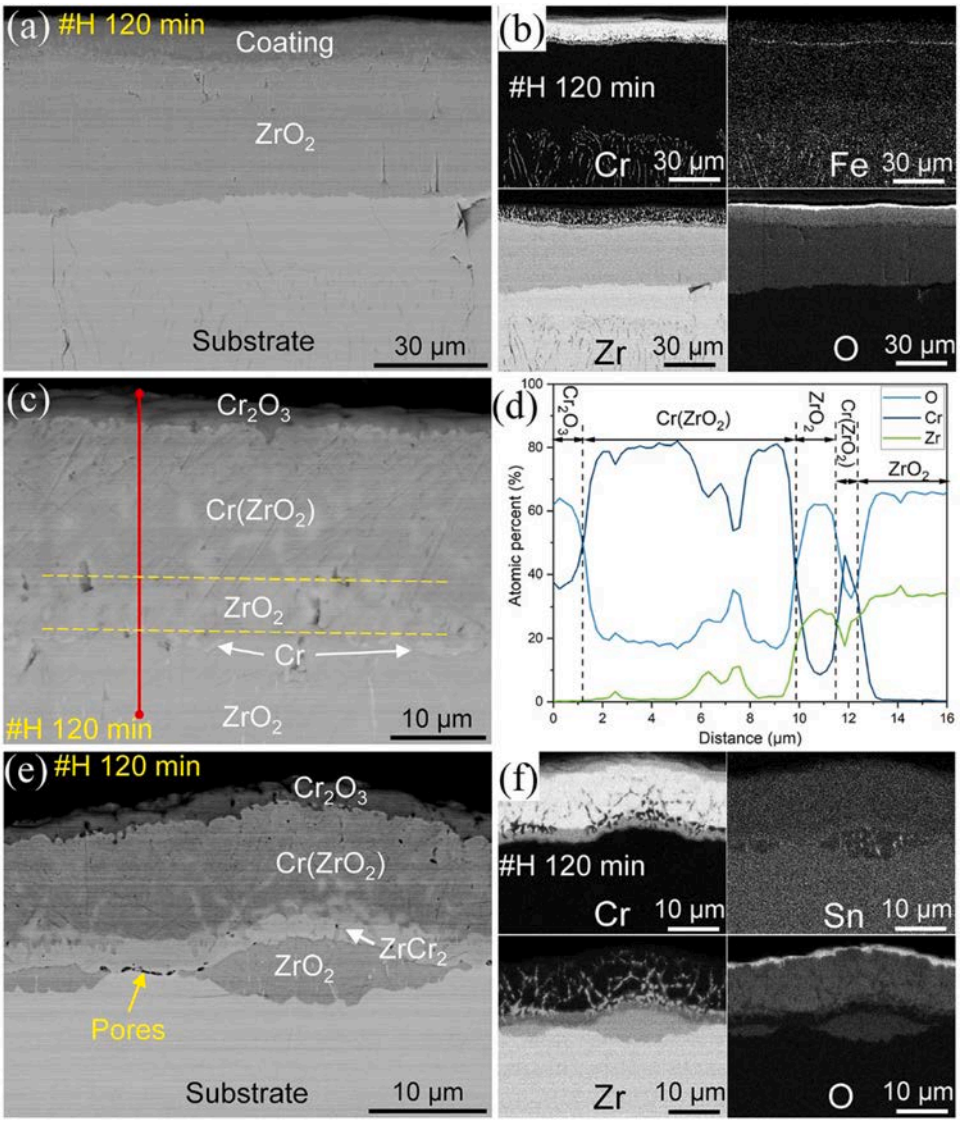

Fig. 10. The cross-sectional SEM images of the Cr-coated Zry-4 samples after steam oxidation: (a) BSE image of the #H sample in small magnification; (b) EDS maps of (a); (c) BSE image of the #H sample in large magnification at the position that the substrate has been oxidized; (d) EDS line scans at the position of red line in (c); (e) BSE image of the #H sample at the position that the substrate has not been totally oxidized; (f) EDS maps of (e).

observed in our previous work [23]. As shown in Fig. 10(e) and (f), at local regions of the #H sample, the oxidation of the substrate is directly related to the outward diffusion of Zr inside the Cr layer. There are ZrO_2 networks distributed above the position where the substrate has been oxidized, and these networks connect the outer Cr_2O_3 scale and the inner substrate. Although there are ZrO_2 precipitates distributed inside the Cr coating above the position of the unoxidized substrate, these ZrO_2 precipitates do not connect the outer Cr_2O_3 scale and the inner substrate. This indicates that the formation of inner ZrO_2 diffusion paths is a necessary condition for the coating degradation and failure. Moreover, in Fig. 10(e), there are pores distributed at the $ZrCr_2$/Zry-4 interface. The formation of this type of pores is also observed and discussed in our previous work [22]. These small interfacial pores inhibit the outward diffusion of Zr to some extent. White particles are observed inside the oxidized substrate, which are mainly Sn-rich precipitates according to the EDS maps in Fig. 10(f). Such precipitates were widely reported by other researchers during the oxidation or corrosion of the Sn-containing Zircaloy [31–33].

3.4. The TEM characterization of the #G sample after oxidation for 90 min

To further investigate the microstructures of the Cr_2O_3/Cr interface and the Cr_2O_3 scale, TEM characterization was conducted. Two TEM specimens were prepared by FIB on both surfaces of the #G sample due to their different microstructures after oxidation (see in Fig. 6(e) and (f)). Fig. 11 shows the TEM micrographs of the specimen prepared at the surface with thin oxide scale together with the SEM images during the thinning of the TEM specimen by FIB. As can be seen in Fig. 11(a)—(c), pores are observed inside the Cr_2O_3 scale and at the Cr_2O_3/Cr interface. It must be emphasized here that Cr is also present above the interfacial pores. This result is different from our previous work according to which pores are distributed only at the Cr_2O_3/Cr interface [22]. It should be related to the oxidation time and oxidation process. Interestingly, there are ZrO_2 precipitates distributed beneath the interfacial pores, and when no interfacial pores appear, no ZrO_2 precipitates exist inside the Cr coating. Moreover, pores inside the Cr_2O_3 scale are only distributed above the position of the interfacial pores and ZrO_2 precipitates. As can be seen in Fig. 11(d)—(f), the ZrO_2 precipitates on the grain boundary of the Cr coating are in monoclinic phase and there is a typical twins

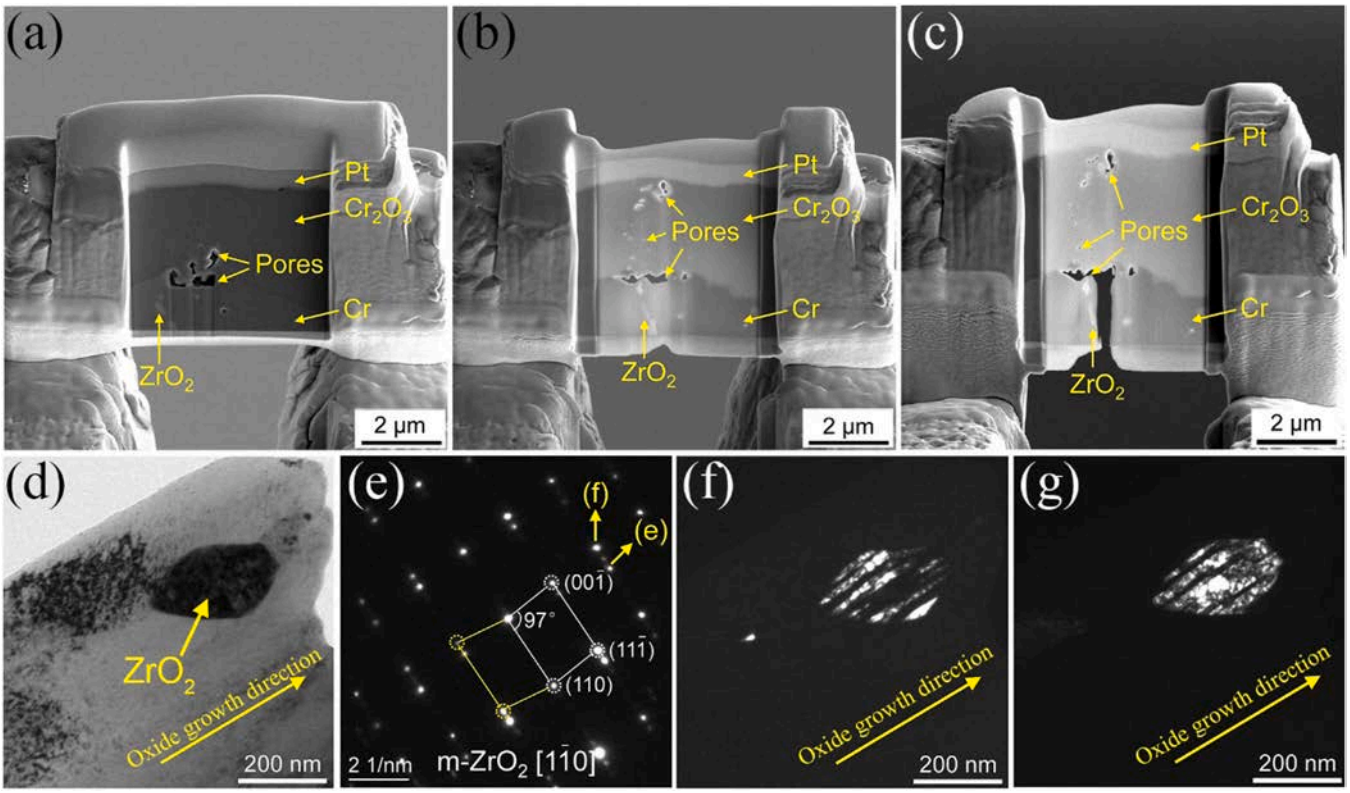

Fig. 11. TEM micrographs of the specimen prepared on the surface with thin oxide scale: (a)—(c) the SEM images of the TEM specimen during the thinning process by FIB; (d) the bright field image of the ZrO_2 precipitate on the Cr grain boundaries; (e) the SAED pattern of the ZrO_2 precipitate in (d); (f) and (g) the dark field image of the ZrO_2 precipitate in (d).

structure inside the ZrO_2 precipitate according to the selected area electron diffraction (SAED) pattern (Fig. 11(e)) and the dark filed images (Fig. 11(f) and (g)). The formation of twins indicates large stress existing inside the ZrO_2 precipitates during oxidation [34–36].

Fig. 12 shows the TEM micrographs of the specimen prepared at the surface with thick oxide scale. Because of the thick oxide layer and the limited depth of FIB (~4 μm), this TEM specimen only contains the outer Cr_2O_3 scale. As can be seen in the scanning transmission electron microscopy (STEM) micrograph in Fig. 12(a), the Cr_2O_3 grains are in equiaxed shape and are densely arranged. However, pores are distributed inside the grains and at the grain boundaries of Cr_2O_3. Locally, the pores are very large and extend along the growth direction of the oxide scale. These large pores should be the linear pores observed by SEM in Fig. 8(e). Fig. 12(b) shows the bright field image with large magnification at the region of these pores. The grain close to the pores is identified as Cr_2O_3 phase by SAED pattern. Moreover, according to the high resolution transmission electron microscopy (HRTEM) image in Fig. 12(c), the edge region of the Cr_2O_3 grain close to the pores transformed into an amorphous structure. This type of amorphous structure could be further verified by the fast Fourier transform (FFT) pattern at the region close to pores in Fig. 12(c). The FFT pattern shows the typical diffraction ring of an amorphous phase. The amorphization of the Cr_2O_3 grains was also observed and discussed in our previous work [22] during the steam oxidation of Cr-coated Zircaloy, and all the amorphous Cr_2O_3 phases in

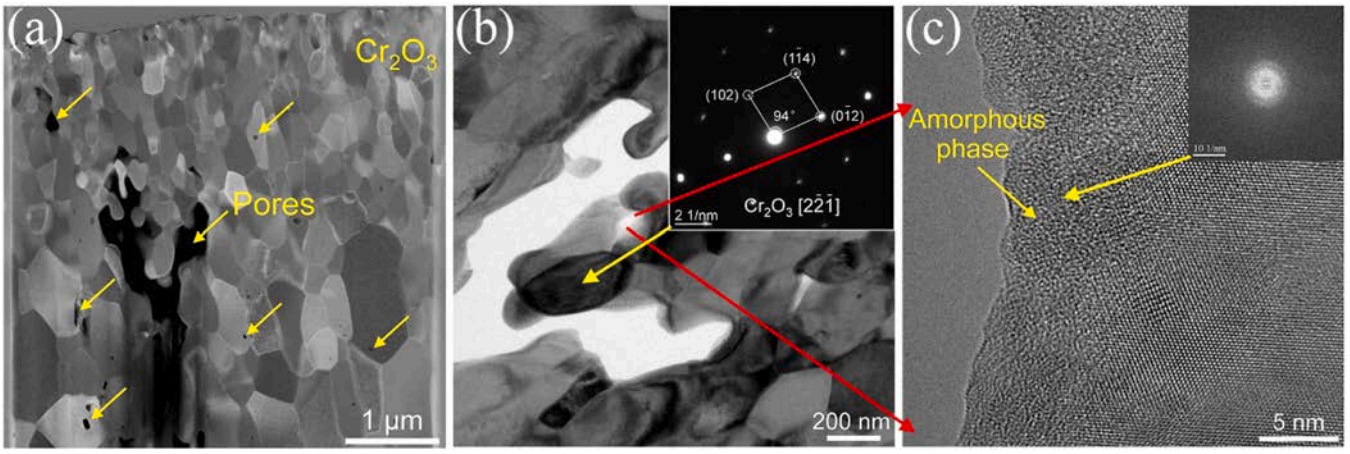

Fig. 12. TEM micrographs of the specimen prepared on the surface with thick oxide scale: (a) STEM image of the whole TEM specimen; (b) bright field image of the Cr_2O_3 scale together with the SAED pattern of the Cr_2O_3 grain; (c) HRTEM image of the region close to the pores and the corresponding FFT pattern.

these two cases are adjacent to the pores.

4. Discussion

According to the experimental results, the oxidation and degradation behavior of the Cr-coated Zry-4 during the isothermal oxidation at 1200 °C can be divided into four stages, depending on the oxidation time:

Stage I: before transition, oxidation time 5–30 min. The coating is protective.

Stage II: transition, oxidation time ~30 min. The coating begins to lose its protection.

Stage III: after transition but before coating failure, oxidation time 30–90 min. The coating has partially lost its protective effect and α-Zr (O) phase formed in the substrate.

Stage IV: coating failure, oxidation time 90–120 min. The coating has completely lost protection resulting in oxidation of the substrate and ZrO_2 formation.

4.1. The oxidation mechanism before transition

Fig. 13(a) shows a schematic of the typical microstructure of the Cr-coated Zircaloy before transition during the isothermal steam oxidation. In the stage before transition, the oxidation and degradation behavior of the Cr-coated Zry-4 consists of the formation and thickening of the Cr_2O_3 scale (Fig. 4 and Fig. 5), the inward diffusion of Cr from the coating into the substrate (Fig. 4(e)), the outward diffusion of Zr along the grain boundaries of Cr (Fig. 4(e)—(g)), as well as the formation and thickening of the $ZrCr_2$ (or $Zr(Cr, Fe)_2$ laves phase [37,38]) layer (Fig. 4 and Fig. 5). This has been discussed in detail in our previous work [23] and in the work of other researchers [20,25,39]. The oxidation of the Cr coating is mainly dominated by the outward diffusion of Cr^{3+} and new oxide grains formed at the gas/Cr_2O_3 interface. Minimal O can also diffuse into the coating from the atmosphere via grain boundaries [22,23].

Before transition, the outward diffusion of Zr and the position of ZrO_2 inside the Cr coating has not reached the Cr_2O_3/Cr interface (Fig. 4 (e)—(g)). In this stage, see also Fig. 13(a), Zr diffuses from the substrate towards the Cr_2O_3/Cr interface along the grain boundaries of the Cr coating, and should be further oxidized mainly by O which diffuses from the outer atmosphere through the Cr_2O_3 scale or O which was dissolved in the Cr coating [25,28].

4.2. The oxidation kinetics transition mechanism

Fig. 13(b) shows a schematic of the typical microstructure of the Cr-coated Zircaloy during transition. On the basis of the results in Section 3.3.2, the absorption of O by the Zircaloy substrate and the formation of α-Zr(O) phase in the substrate lead to the transition of the oxidation kinetics. The same conclusion was also obtained by other researchers [25]. Furthermore, in the current experiments, the inward diffusion of O through the coating to the substrate should be directly attributed to two phenomena: the thickness decrease of the outer Cr_2O_3 scale and the formation of ZrO_2 precipitates inside the Cr coating, which connect the outer Cr_2O_3 scale and inner substrate and act as O diffusion paths. The first phenomenon accelerates the inward diffusion of O from the outer atmosphere to the inner coating while the second phenomenon facilitates the inward diffusion of oxygen from the inner coating to the Zircaloy substrate. Eventually, a lot of O diffuses into the substrate and leads to the occurrence of the transition. The thickness of the α-Zr(O) layer in the substrate depends on the thickness of the outer Cr_2O_3 scale

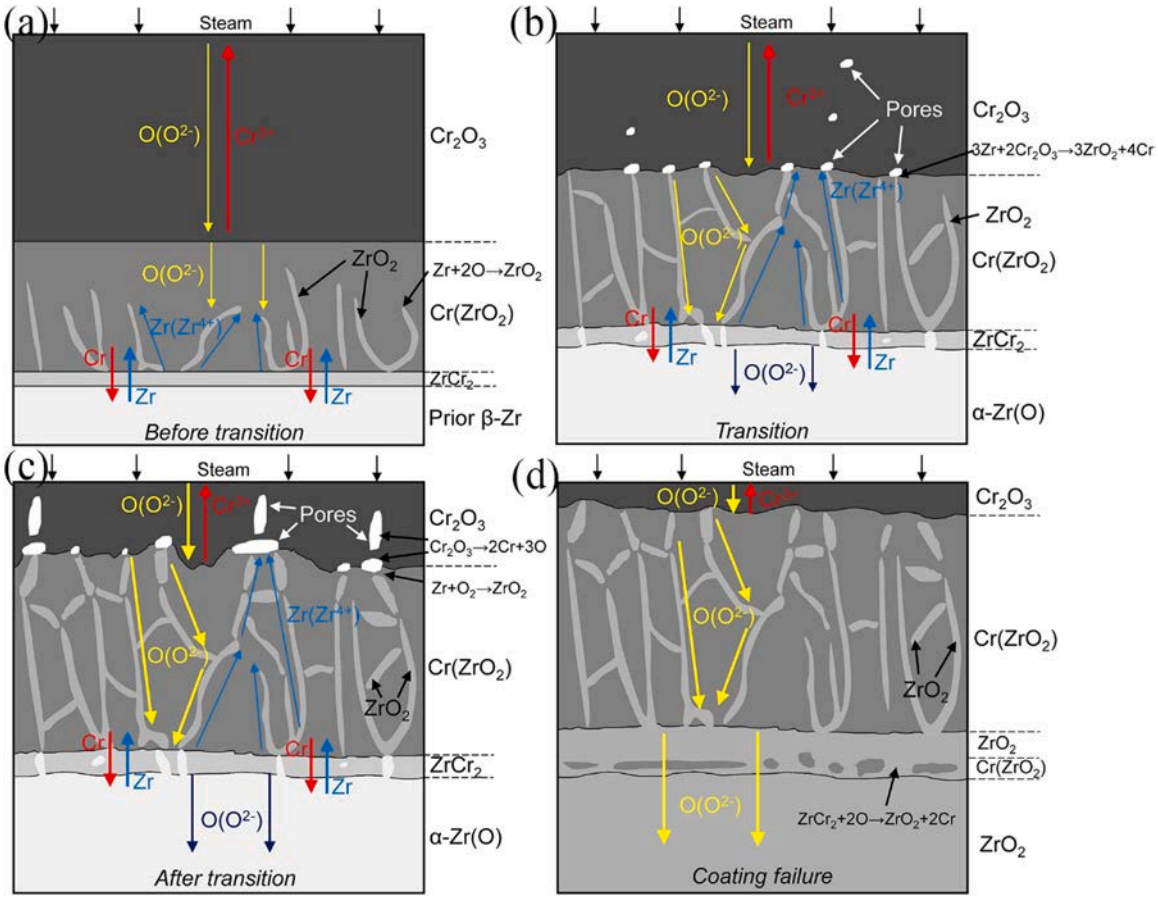

Fig. 13. Schematic of the microstructural evolution of the Cr-coated Zircaloy during isothermal steam oxidation: (a) before transition; (b) transition; (c) after transition; (d) coating failure.

(Fig. 6) which determines the amount of O diffusing into the inner coating from the atmosphere through the Cr_2O_3 scale. When the transition occurs, although significant amount of O diffuses into the Zircaloy substrate, the O flow is still limited and the concentration of O in the Zry-4 substrate has not reached its solubility limit. Therefore, only the α-Zr(O) phase forms and the ZrO_2 phase cannot nucleate in the substrate, which indicates the surface coating has not entirely lost its protection.

All evidence in the results show that the thickness decrease of the Cr_2O_3 scale is a consequence of the outward diffusion of Zr. Before transition, Zr has not diffused to the Cr_2O_3/Cr interface and there is no reduction of the Cr_2O_3 (Fig. 5). Nevertheless, when Zr/ZrO_2 reaches the Cr_2O_3/Cr interface, the thickness of the Cr_2O_3 scale rapidly decreases (Fig. 5) and the Cr_2O_3/Cr interface transforms from flat to wavy (Fig. 7). Moreover, after transition, only ZrO_2 precipitates/networks are observed beneath the thinner Cr_2O_3 scale (Fig. 8(d)) and beneath the wave crest of the wavy Cr_2O_3/Cr interface (Fig. 8(f)). This indicates that the reaction between the outward diffused Zr and the Cr_2O_3 scale is likely to be the most important factor for the thickness decrease of the Cr_2O_3 scale, see Fig. 13(b). This reaction consumes Cr_2O_3 but produces ZrO_2 and Cr. Therefore, when Zr reaches the Cr_2O_3/Cr interface, O from Cr_2O_3 is another source for the oxidation of Zr besides the O diffusing from the atmosphere through the Cr_2O_3 scale. The above-mentioned explanation about the reduction mechanism of Cr_2O_3 scale is different from the interpretation in the paper of Han et al. [20,21] that the Cr_2O_3 scale is reduced by the Zircaloy substrate. This difference should be attributed to the different phenomena observed in the current experiments with sudden heating-up of the samples before oxidation: 1) the Cr_2O_3 scale begins to reduce even if a certain thick unoxidized Cr layer remains beneath the Cr_2O_3 scale in the current experiments, while in the work of Han et al. the thickness of the Cr_2O_3 scale begins to decrease after the Cr coating is completely oxidized. 2) In this paper, there is no ZrO_2 layer formed in the substrate when the thickness of the Cr_2O_3 scale begins to decrease, while a ZrO_2 layer was observed in the work of Han et al. The formation of ZrO_2 and Cr by the reaction between Zr and Cr_2O_3 should lead to the thickness increase of the Cr(ZrO_2) layer. However, the thickness of the Cr(ZrO_2) layer does not change too much when transition occurs (Fig. 5), and this should be due to the gradual inward diffusion of Cr from the Cr(ZrO_2) layer to the substrate.

When transition occurs, a lot of Zr diffuses into the $ZrCr_2$ layer from the substrate and further accumulates inside the $ZrCr_2$ layer and eventually leads to the transformation of the continuous $ZrCr_2$ layer to a discontinuous one (Fig. 13(b)). The Zr particles inside the $ZrCr_2$ layer as well as the gaps inside the $ZrCr_2$ layer always appear beneath the outer ZrO_2 precipitates (Fig. 7(b) and (f)) can provide evidence for this hypothesis.

4.3. The oxidation mechanism after transition but before total coating failure

After transition, when oxidation time increased from 45 min to 90 min in our experiments, the average thickness of the outer Cr_2O_3 scale does not change too much (Fig. 5). In this stage, as shown in Fig. 13 (c), pores formed at the Cr_2O_3/Cr interface. This type of interfacial pores was also observed in our previous work [22] and the formation mechanism was interpreted as the vacancy condensation [40,41] at the Cr_2O_3/Cr interface. Fig. 14 shows the schematic of the oxidation mechanism of the Cr-coated Zircaloy and the formation mechanism of the interfacial pores. During oxidation, the Cr^{3+} vacancies diffuse from the Cr_2O_3/gas interface to the Cr_2O_3/Cr interface, meanwhile, O^{2-} vacancies diffuse from the ZrO_2 precipitates inside the Cr coating layer to the Cr_2O_3/Cr interface. The condensation of Cr^{3+} vacancies and O^{2-} vacancies at the Cr_2O_3/Cr interface can result in the nucleation and formation of pores. Besides the vacancy condensation, the reaction between Zr and Cr_2O_3 scale below should be another reason for the formation of pores in this work:

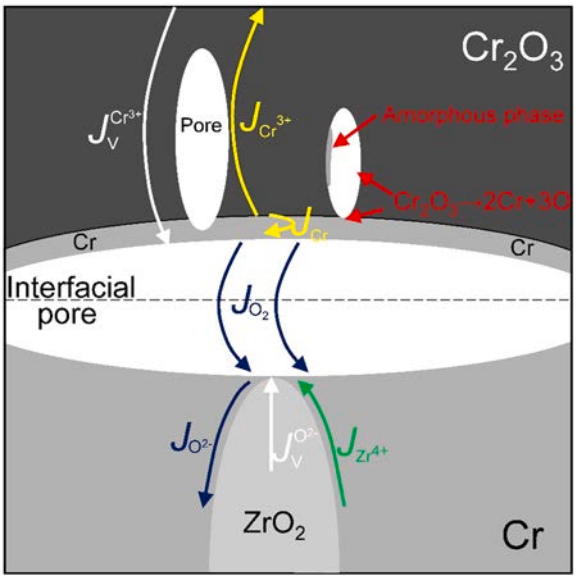

Fig. 14. Schematic of the oxidation mechanism of the Cr-coated Zircaloy when pores form on the Cr_2O_3/Cr interface.

$$2Cr_2O_3 + 3Zr \rightarrow 3ZrO_2 + 4Cr \quad (1)$$

The Pilling-Bedworth ratios (PBR) during the formation of Cr_2O_3 and ZrO_2 are 2.07 [42] and 1.56 [43], respectively. Theoretically, the consumption of 1 mol Cr_2O_3 can produce 1.5 mol ZrO_2 (Fig. 13(b)), and as a result, there will be a small volume expansion when the transformation of Cr_2O_3 to ZrO_2 occurs. However, in the actual oxidation process, as can be seen in Fig. 11(d), the ZrO_2 precipitates always form on the grain boundaries of the Cr coating, which indicates the volume expansion of ZrO_2 during the oxidation can be effectively constrained by the Cr grain boundaries. The appearance of the twins in these ZrO_2 precipitates (Fig. 11(e)—(g)) provides evidence that a large compression stress exists inside the ZrO_2 precipitates. Therefore, the volume expansion during the formation of ZrO_2 precipitates on the Cr grain boundaries cannot compensate the volume loss during the decomposition of the Cr_2O_3, and pores form at the Cr_2O_3/Cr interface. However, when Zr diffuses out of the grain boundaries of the Cr coating to the inner surface of the pores, the volume of ZrO_2 can expand freely and the formation of ZrO_2 can heal the pores.

When pores form at the Cr_2O_3/Cr interface, the original oxidation mechanism of the Cr-coated Zry-4 should be affected. Firstly, the reaction rate between Zr and Cr_2O_3 in Eq. 1 decreases because there is no direct interaction between Zr and Cr_2O_3. Secondly, the outward diffusion of Cr from the unoxidized Cr coating to the outer Cr_2O_3 scale is restrained. Thirdly, as discussed in our previous work [22], the decomposition of Cr_2O_3 close to the pores occurs and follows the reaction below:

$$Cr_2O_3 \rightarrow 3O + 2Cr \quad (2)$$

As shown in Fig. 14, the complete decomposition of Cr_2O_3 close to the pores produces Cr and O. Partially Cr loses electrons to generate Cr^{3+} which further diffuses outward to the outer surface and generates new Cr_2O_3 grains at the Cr_2O_3/gas interface. If the formation rate of Cr (J_{Cr}) produced by Eq. 2 is larger than the flow rate of the Cr^{3+} (J_{Cr}^{3+}), which diffuses towards to the outer surface of the coating, a small amount of Cr accumulates above the pores (Fig. 11 (a)—(c)). In this stage, Cr_2O_3 decomposes at the Cr_2O_3/Cr interface with a relatively lower decomposition rate compared with the reduction rate of the Cr_2O_3 by direct reaction between Zr and Cr_2O_3. At the same time, new oxide layer forms at the Cr_2O_3/gas interface. Consequently, the thickness of the Cr_2O_3 scale does not significantly decrease during the oxidation from 45 min to

90 min. Oxygen produced by the decomposition of Cr_2O_3 in Eq. 1 further diffuses to the substrate through the interfacial pores as molecular gas and reacts with Zr inside the Cr coating beneath the pores. This oxygen diffusion mechanism through pores was proposed and discussed in our previous paper in detail [22]. The further oxidation of Zr and the formation of ZrO_2 inside the Cr coating can lead to a slight thickness increase of the unoxidized Cr coating when oxidation time increases from 45 min to 90 min in Fig. 5. In our previous work [23], we have confirmed that the oxidation of Zr in Cr coating can significantly cause a thickness growth of the Cr layer (~32%).

In addition, pores are also observed inside the Cr_2O_3 scale at this stage (Fig. 13(c)), and the concentration of pores increases with longer oxidation time (Fig. 7 and Fig. 8). It should be noted that these pores inside the Cr_2O_3 scale distribute just above the pores at the Cr_2O_3/Cr interface and above the ZrO_2 precipitates/networks inside the unoxidized Cr coating. This indicates that the formation of pores inside the Cr_2O_3 scale is also related to the outward diffusion of Zr along the Cr grain boundaries. According to the TEM results in Fig. 12, amorphous phase is distributed along the edge of the Cr_2O_3 grains close to the pores. This type of amorphization of Cr_2O_3 close to the pores was also observed in our previous paper and the amorphization mechanism should be attributed to the incomplete decomposition of Cr_2O_3 grains [22]. The evaporation of O inside the Cr_2O_3 grains lead to the formation of oxygen vacancies as followed in the equation below:

$$O^{2-} \rightarrow O_{\square}^{2+} + \frac{1}{2}O_2 + 2e \quad (3)$$

where $O_{\square}^{2+}$ is an oxygen vacancy. The formation of oxygen vacancies in Cr_2O_3 can lead to the order-disorder transformation of the Cr_2O_3 grains. In this paper it is shown that the complete decomposition of Cr_2O_3 in Eq. 2 produces pores inside the Cr_2O_3 scale, while the incomplete decomposition of Cr_2O_3 in Eq. 3 causes the formation of amorphous Cr_2O_3 phase (Fig. 12(c)).

There is no significant microstructural evolution about the $ZrCr_2$ layer at this stage. The morphology of the Cr-rich precipitates inside the Zircaloy substrate transforms from small particles to large club shaped ones, which indicates the gradual inward diffusion of Cr in the Zircaloy substrate. After oxidation for 90 min, Fe in the substrate also segregates in these Cr-rich precipitates, which was also reported in our previous work [23].

4.4. The coating failure mechanism

When exposed to steam for 120 min, wide coating failure occurs resulting in fast oxidation of the substrate. Here the coating failure does not indicate the cracking or the spallation of the coating, because in the actual experiments, even when the substrate is oxidized no obvious cracking or spallation of the coating was observed. Therefore, the coating failure is just attributed to the loss of the structural integrity and the loss of the protective function of the coating. After oxidation for 120 min, the thickness of the Cr_2O_3 scale significantly decreased (Fig. 10) and only a very thin Cr_2O_3 scale ($\leq$ ~2 μm) remained on the outer surface of the coating. Besides, many ZrO_2 precipitates/networks are distributed inside the unoxidized Cr coating. As a result, more O diffuses into the substrate and the concentration of O reaches the solubility limit of O in Zry-4. As a result, ZrO_2 nucleates in the substrate and the oxidation of the substrate occurs.

As shown in Fig. 10(c), when the oxidation of the substrate occurs, pores at the Cr_2O_3/Cr interface can hardly be seen. This indicates that these interfacial pores should be filled by the oxidation of the inner Zr in the Cr coating. In the later stages of oxidation, when Zr diffuses to the inner surface of the pores and the oxidation of Zr no longer occurs on the Cr grain boundaries, the volume expansion during the oxidation of Zr can gradually heal the interfacial pores. The tendency of the filling of the interfacial pores by ZrO_2 was observed in our previous work [22] showing an individual small jutting ZrO_2 grain distributed on the inner surface of the interfacial pores. Moreover, the healing of the interfacial pores was also reported by other researchers [44] during the oxidation of NiAl alloys. When the concentration of the pores at the Cr_2O_3/Cr interface decreases, the reaction rate between Zr and Cr_2O_3 and the inward diffusion rate of O is increased, which should be an important reason for the rapid thickness decrease of the Cr_2O_3 scale and the coating failure in this stage.

After coating failure, as can be seen in Fig. 13(d), the $ZrCr_2$ layer was partially oxidized and converted into ZrO_2 and Cr. The oxidation of Zircaloy substrate precedes the oxidation of the remaining Cr in the coating due to the larger oxygen affinity of Zr compared with Cr (the standard Gibbs formation energies per mole of O_2 of ZrO_2 and Cr_2O_3 are 821 and 505 kJ/mol at 1200 °C [45,46], respectively). According to our previous work [23], the remaining Cr in the coating will be further oxidized into Cr_2O_3 and the Cr coating eventually transforms into a mixed oxide layer of Cr_2O_3 and ZrO_2 when the inner ZrO_2 layer in the substrate has grown to a certain thickness.

5. Conclusions

The isothermal oxidation behavior of the Cr-coated Zry-4 sheet samples at 1200 °C under steam atmosphere was extensively investigated. The relationships between the thickness decrease of the Cr_2O_3 scale, the outward diffusion and selective oxidation of Zr along the Cr grain boundaries, and the microstructural evolution of the pores on the Cr_2O_3/Cr interface are discussed. Based on the results obtained with various examination methods, coating degradation and oxidation kinetics transition mechanisms are proposed. Several crucial conclusions are drawn from the obtained results:

(1) The oxidation kinetics transition of the Cr-coated Zircaloy should be attributed to the combined effects of the thickness decrease of the Cr_2O_3 scale and the formation of ZrO_2 networks inside the unoxidized Cr coating.
(2) The outward diffused Zr on the Cr grain boundaries reacts with the Cr_2O_3 scale as Zr reaches the Cr_2O_3/Cr interface, and this reaction further leads to the thickness decrease of the Cr_2O_3 scale.
(3) When the thickness of the outer Cr_2O_3 scale decreases to a very small value ($\leq$ ~2 μm), the coating failure occurs and the substrate beneath the coating is oxidized.
(4) The formation of the pores at the Cr_2O_3/Cr interface is caused by vacancy condensation and the reaction between Zr and Cr_2O_3. These pores alter the reaction mechanism of the Cr-coated Zry-4.
(5) Pores are also observed inside the Cr_2O_3 scale after transition. These pores are just distributed above the interfacial pores. The amorphization of Cr_2O_3 grains occurs close to the pores. The formation of these pores could be attributed to the decomposition of Cr_2O_3 grains.
(6) The thickness of the $ZrCr_2$ layer gradually increases before transition. Then after transition, the continuous $ZrCr_2$ layer transforms to a discontinuous one. After coating failure, the $ZrCr_2$ layer is finally converted into ZrO_2 and Cr.

Finally, it should be mentioned that the results presented here are of general validity, but the times for the individual degradation phases should depend on the thickness and morphology of the Cr coating used. Hence, the effect of coating deposition methods and coating microstructures on the coating degradation behavior need to be further investigated.

CRediT authorship contribution statement

Junkai Liu : Conceptualization, Methodology, Investigation, Writing – original draft. **Martin Steinbrück:** Conceptualization, Project administration, Writing – review & editing. **Mirco Große:**

Conceptualization, Writing – review & editing. **Ulrike Stegmaier:** Investigation, Writing – review & editing. **Chongchong Tang:** Investigation, Methodology, Writing – review & editing. **Di Yun:** Supervision. **Jianqiao Yang:** Resources. **Yanguang Cui:** Project administration. **Hans Jürgen Seifert:** Supervision.

Declaration of Competing Interest

The authors declare that they have no known competing financial interests or personal relationships that could have appeared to influence the work reported in this paper.

Data Availability

The raw data required to reproduce these findings cannot be shared at this time as the data also forms part of an ongoing study. The processed data required to reproduce these findings cannot be shared at this time as the data also forms part of an ongoing study.

Acknowledgements

Junkai Liu is supported by the China Scholarship Council (No. 201906280379), China. Financial support provided by the National Science and Technology Major Project (No. 2019ZX06002001), China. The work was conducted in the framework of the HGF program NUSAFE, Germany. The authors thank Petra Severloh for her support in the sample preparation and optical metallography investigations.

References

[1] J.K. Liu, X.H. Zhang, D. Yun, A complete review and a prospect on the candidate materials for accident-tolerant fuel claddings, Mater. Rev. 32 (2018) 1757–1778.
[2] K.A. Terrani, Accident tolerant fuel cladding development: Promise, status, and challenges, J. Nucl. Mater. 501 (2018) 13–30.
[3] S.J. Zinkle, K.A. Terrani, J.C. Gehin, L.J. Ott, L.L. Snead, Accident tolerant fuels for LWRs: A perspective, J. Nucl. Mater. 448 (2014) 374–379.
[4] L.J. Ott, K.R. Robb, D. Wang, Preliminary assessment of accident-tolerant fuels on LWR performance during normal operation and under DB and BDB accident conditions, J. Nucl. Mater. 448 (2014) 520–533.
[5] C. Tang, M. Stueber, H.J. Seifert, M. Steinbrueck, Protective coatings on zirconium-based alloys as accident-tolerant fuel (ATF) claddings, Corros. Rev. 35 (2017) 141–165.
[6] J. Yang, M. Steinbrück, C. Tang, M. Große, J. Liu, J. Zhang, D. Yun, S. Wang, Review on chromium coated zirconium alloy accident tolerant fuel cladding, J. Alloy Compd. 895 (2022), 162450.
[7] J. Liu, Z. Cui, D. Ma, J. Lu, Y. Cui, C. Li, W. Liu, Z. Hao, P. Hu, M. Yao, Investigation of oxidation behaviors of coated Zircaloy as accident-tolerant fuel with CrAlN and CrAlSiN coatings in high-temperature steam, Corres. Sci. 175 (2020), 108896.
[8] C. Tang, M. Steinbrueck, M. Stueber, M. Grosse, X. Yu, S. Ulrich, H.J. Seifert, Deposition, characterization and high-temperature steam oxidation behavior of single-phase Ti 2 AlC-coated Zircaloy-4, Corres. Sci. 135 (2018) 87–98.
[9] C. Tang, M. Große, S. Ulrich, M. Klimenkov, U. Jantsch, H.J. Seifert, M. Stüber, M. Steinbrück, High-temperature oxidation and hydrothermal corrosion of textured Cr2AlC-based coatings on zirconium alloy fuel cladding, Surf. Coat. Technol. 419 (2021), 127263.
[10] D. Jin, N. Ni, Y. Guo, Z. Zou, X. Wang, F. Guo, X. Zhao, P. Xiao, Corrosion of the bonding at FeCrAl/Zr alloy interfaces in steam, J. Nucl. Mater. 508 (2018) 411–422.
[11] G. Li, C. Cai, Y. Wang, Y. Zhou, L. Yang, J. Lu, G. Zhou, Zirconium silicate growth induced by the thermochemical interaction of yttria-stablized zirconia coatings with molten CMAS deposits, Corres. Sci. 149 (2019) 249–256.
[12] Y.J. Park, J.W. Kim, G. Ali, S.O. Cho, Enhancement of oxidation resistance of zirconium alloy with anodic nanoporous oxide layer in high-temperature air/steam environments, Corros. Sci. 140 (2018) 217–222.
[13] J.G. Gigax, M. Kennas, H. Kim, T. Wang, B.R. Maier, H. Yeom, G.O. Johnson, K. Sridharan, L. Shao, Radiation response of Ti2AlC MAX phase coated Zircaloy-4 for accident tolerant fuel cladding, J. Nucl. Mater. 523 (2019) 26–32.
[14] J. Brachet, I. Idarraga-Trujillo, M. Le Flem, M. Le Saux, V. Vandenberghe, S. Urvoy, E. Rouesne, T. Guilbert, C. Toffolon-Masclet, M. Tupin, Early studies on Cr-Coated Zircaloy-4 as enhanced accident tolerant nuclear fuel claddings for light water reactors, J. Nucl. Mater. 517 (2019) 268–285.
[15] H. Kim, I. Kim, Y. Jung, D. Park, J. Park, Y. Koo, Adhesion property and high-temperature oxidation behavior of Cr-coated Zircaloy-4 cladding tube prepared by 3D laser coating, J. Nucl. Mater. 465 (2015) 531–539.
[16] F. Qi, Z. Liu, Q. Li, H. Yu, P. Chen, Y. Li, Y. Zhou, C. Ma, C. Tang, Y. Huang, Pellet-cladding mechanical interaction analysis of Cr-coated Zircaloy cladding, Nucl. Eng. Des. 367 (2020), 110792.
[17] J.C. Brachet, M. Dumerval, V. Lezaud-Chailioux, M. Le Saux, E. Rouesne, D. Hamon, S. Urvoy, T. Guilbert, Q. Houmaire, C. Cobac, Behavior of chromium coated M5TM claddings under LOCA conditions, WRFPM 2017 Water Reactor Fuel Performance Meeting, WRFPM 2017 Water Reactor Fuel Performance Meeting, 2017.
[18] L.B. Begrambekov, A.E. Evsin, A.V. Grunin, A.I. Gumarov, A.S. Kaplevsky, N. F. Kashapov, A.G. Luchkin, I.R. Vakhitov, I.V. Yanilkin, L.R. Tagirov, Irradiation with hydrogen atoms and ions as an accelerated hydrogenation test of zirconium alloys and protective coatings, Int. J. Hydro. Energy 44 (2019) 17154–17162.
[19] A.S. Kuprin, V.A. Belous, V.N. Voyevodin, R.L. Vasilenko, V.D. Ovcharenko, G. D. Tolstolutskaya, I.E. Kopanets, I.V. Kolodiy, Irradiation resistance of vacuum arc chromium coatings for zirconium alloy fuel claddings, J. Nucl. Mater. 510 (2018) 163–167.
[20] X. Han, C. Chen, Y. Tan, W. Feng, S. Peng, H. Zhang, A systematic study of the oxidation behavior of Cr coatings on Zry4 substrates in high temperature steam environment, Corros. Sci. 174 (2020), 108826.
[21] X. Han, J. Xue, S. Peng, H. Zhang, An interesting oxidation phenomenon of Cr coatings on Zry-4 substrates in high temperature steam environment, Corres. Sci. 156 (2019) 117–124.
[22] J. Liu, Z. Cui, Z. Hao, D. Ma, J. Lu, Y. Cui, C. Li, W. Liu, S. Xie, P. Hu, Steam oxidation of Cr-coated Sn-containing Zircaloy solid rod at 1000° C, Corros. Sci. (2021), 109682.
[23] J. Liu, C. Tang, M. Steinbrück, J. Yang, U. Stegmaier, M. Große, D. Yun, H. J. Seifert, Transient experiments on oxidation and degradation of Cr-coated Zircaloy in steam up to 1600℃, Corros. Sci. 192 (2021), 109805.
[24] J.C. Brachet, T. Guilbert, M. Lesaux, J. Rousselot, G. Nony, C. Toffolon-Masclet, F. Schuster, H. Palancher, J. Bischoff, J. Augereau, Behavior of cr-coated m5 claddings during and after high temperature steam oxidationfrom 800c up to 1500c, Topfuel 2018, Topfuel 2018, 2018.
[25] J. Brachet, E. Rouesne, J. Ribis, T. Guilbert, S. Urvoy, G. Nony, C. Toffolon-Masclet, M. Le Saux, N. Chaabane, H. Palancher, A. David, J. Bischoff, J. Augereau, E. Pouillier, High temperature steam oxidation of chromium-coated zirconium-based alloys: kinetics and process, Corros. Sci. 167 (2020), 108537.
[26] H. Ma, J. Yan, Y. Zhao, T. Liu, Q. Ren, Y. Liao, J. Zuo, G. Liu, M. Yao, Oxidation behavior of Cr-coated zirconium alloy cladding in high-temperature steam above 1200C, npj Mater. Degrad. 5 (2021) 1–11.
[27] M. Steinbrück, Oxidation of boron carbide at high temperatures, J. Nucl. Mater. 336 (2005) 185–193.
[28] J. Yang, U. Stegmaier, C. Tang, M. Steinbrück, M. Große, S. Wang, H.J. Seifert, High temperature Cr-Zr interaction of two types of Cr-coated Zr alloys in inert gas environment, J. Nucl. Mater. 547 (2021), 152806.
[29] X. He, Z. Tian, B. Shi, X. Xu, C. Meng, W. Dang, J. Tan, X. Ma, Effect of gas pressure and bias potential on oxidation resistance of Cr coatings, ANN Nucl. Energy 132 (2019) 243–248.
[30] T. Wei, R. Zhang, H. Yang, H. Liu, S. Qiu, Y. Wang, P. Du, K. He, X. Hu, C. Dong, Microstructure, corrosion resistance and oxidation behavior of Cr-coatings on Zircaloy-4 prepared by vacuum arc plasma deposition, Corros Sci 158 (2019), 108077.
[31] C.M. Lee, D. Sohn, Enhanced high-temperature oxidation resistance of a zirconium alloy cladding by high-temperature preformed oxide on the cladding, Corros. Sci. 131 (2018) 116–125.
[32] H. Hulme, F. Baxter, R.P. Babu, M.A. Denecke, M. Gass, A. Steuwer, K. Norén, S. Carlson, M. Preuss, An X-ray absorption near-edge structure (XANES) study of the Sn L3 edge in zirconium alloy oxide films formed during autoclave corrosion, Corros. Sci. 105 (2016) 202–208.
[33] M. Grosse, R. Simon, Analysis of tin diffusion in zircaloy-4 and tin redistribution after steam oxidation by means of x-ray fluorescence measurements, Adv. Eng. Mater. 11 (2009) 483–487.
[34] J. Liu, Z. Hao, Z. Cui, D. Ma, J. Lu, Y. Cui, C. Li, W. Liu, S. Xie, P. Hu, P. Huang, G. Bai, D. Yun, Oxidation behavior, thermal stability, and the coating/substrate interface evolution of CrN-coated Zircaloy under high-temperature steam, Corros. Sci. 185 (2021), 109416.
[35] G. Van Tendeloo, L. Anders, G. Thomas, Electron microscopy investigation of the ZrO2-ZrN system—II, Tetragonal monoclinic ZrO2 Precip., Acta Metall. 31 (1983) 1619–1625.
[36] K. Lu, L. Lu, S. Suresh, Strengthening materials by engineering coherent internal boundaries at the nanoscale, Science 324 (2009) 349–352.
[37] J. Ribis, A. Wu, J. Brachet, F. Barcelo, B. Arnal, Atomic-scale interface structure of a Cr-coated Zircaloy-4 material, J. Mater. Sci. 53 (2018) 9879–9895.
[38] A. Wu, J. Ribis, J. Brachet, E. Clouet, F. Leprêtre, E. Bordas, B. Arnal, HRTEM and chemical study of an ion-irradiated chromium/zircaloy-4 interface, J. Nucl. Mater. 504 (2018) 289–299.
[39] H. Yeom, B. Maier, G. Johnson, T. Dabney, M. Lenling, K. Sridharan, High temperature oxidation and microstructural evolution of cold spray chromium coatings on Zircaloy-4 in steam environments, J. Nucl Mater 526 (2019), 151737.
[40] P.Y. Hou, Y. Niu, C. Van Lienden, Analysis of pore formation at oxide–alloy interfaces—I: experimental results on FeAl, Oxid. Met. 59 (2003) 41–61.
[41] S. Taniguchi, D.L. Carpenter, The influence of scale/metal interface characteristics on the oxidation behaviour of iron at elevated temperatures, Corros. Sci. 19 (1979) 15–26.
[42] A.M. Huntz, Stresses in NiO, Cr2O3 and Al2O3 oxide scales, Mater. Sci. Eng.: A 201 (1995) 211–228.
[43] H.X. Zhang, D. Fruchart, E.K. Hlil, L. Ortega, Z.K. Li, J.J. Zhang, J. Sun, L. Zhou, Crystal structure, corrosion kinetics of new zirconium alloys and residual stress analysis of oxide films, J. Nucl. Mater. 396 (2010) 65–70.

[44] H. Svensson, P. Knutsson, K. Stiller, Formation and healing of voids at the metal–oxide interface in NiAl alloys, Oxid. Met. 71 (2009) 143–156.
[45] I. Barin, Thermochemical data of pure substances, VCH, (1989).
[46] J. Liu, Z. Hao, Z. Cui, D. Ma, J. Lu, Y. Cui, C. Li, W. Liu, S. Xie, P. Huang, Investigation of the oxidation mechanisms of superlattice Cr-CrN/TiSiN-Cr multilayer coatings on Zircaloy substrates under high-temperature steam atmospheres, Corros. Sci. 192 (2021), 109782.